Journal of
Materials Chemistry C

PAPER

View Article Online
View Journal

Cite this: DOI: 10.1039/c8tc05580g

Amphiphilic iron(II) spin crossover coordination polymers: crystal structures and phase transition properties†

Johannes Weihermüller,[a] Stephan Schlamp,[a] Wolfgang Milius,[b] Florian Puchtler,[b] Josef Breu,[b] Philipp Ramming,[c] Sven Hüttner,[c] Seema Agarwal,[d] Christoph Göbel,[a] Markus Hund,[e] Georg Papastavrou[e] and Birgit Weber*[a]

Received 6th November 2018,
Accepted 9th December 2018

DOI: 10.1039/c8tc05580g

rsc.li/materials-c

Iron(II) coordination polymers with an N_2O_2 coordinating Schiff base-like equatorial ligand bearing different alkyl chain lengths (C16, C18, C20, and C22) and 1,2-bis(4-pyridyl)ethyne, 1,2-bis(4-pyridyl)ethene or 1,2-bis(4-pyridyl)ethane as bridging ligand are synthesized. All complexes display a rather similar abrupt spin transition above room temperature, which is investigated using magnetic measurements and Mössbauer spectroscopy. Variation of the bridging ligand and the alkyl chain lengths allows fine tuning of the transition temperature in the range between 338 K and 357 K. Single crystal X-ray structure analysis of two coordination polymers and one of the starting complexes reveals the formation of a lipid layer-like arrangement of the amphiphilic complexes in all cases. Further characterization by thermal gravimetric analysis, differential scanning calorimetry, X-ray powder diffraction, and polarized optical microscopy show in all cases solid–solid phase transitions. Those transitions determine the spin crossover behavior and depend on the crystal packing that is controlled by the alkyl chains in the outer periphery of the ligand. Thus, with the presented system the spin crossover properties are controlled by small alterations of the ligand structures. With respect to technological applications, spin coating is shown to be suitable for the processing of the complexes as thin films and furthermore thin platelets of the complexes can be generated by delamination techniques.

1. Introduction

Bistability is a property frequently observed for hexa-coordinated complexes of 3d transition metals with d^4–d^7 electron configuration.[1–3] Through external perturbations like changes in temperature, pressure, by electromagnetic irradiation, or through chemical stimuli, the spin state of the metal center can be switched between a high spin (HS) and a low spin (LS) state, a phenomenon known as spin crossover (SCO). Due to the pronounced property changes upon SCO, these switchable molecular materials have a high potential for a variety of different applications.[4–8] One example would be bio-sensors for nano-thermometry[9–11] or the detection of biologically relevant parameters such as pH. In order to achieve such applications, the synthesis of nanostructured and/or composite materials is investigated very actively.[12–17] Alternatively, attempts are made to combine the SCO with additional properties like softness (metallomesogens, amphiphilic molecules)[18–21] leading to multifunctionality, new patterning possibilities, and by this enlarging the range of potential SCO applications. The structural changes upon spin state change could trigger a LC phase transition or, alternatively, the phase transition could trigger the spin transition.[18,22,23] With regard to this, Seredyuk *et al.* demonstrated that the SCO can be influenced by crystal–liquid crystal phase transitions (PTs) of metal complexes functionalized with long alkyl chain substituents[18,24,25] Hayami and co-workers observed interesting phenomena like a reverse ST due to PTs for amphiphilic cobalt complexes.[22,26] Further approaches by the group of Real yielded scan rate dependent cooperative spin

---

[a] *Department of Chemistry, Inorganic Chemistry VI, Universität Bayreuth, Universitätsstrasse 30, NW I, 95440 Bayreuth, Germany. E-mail: weber@uni-bayreuth.de*
[b] *Department of Chemistry, Inorganic Chemistry I, Universität Bayreuth, Universitätsstrasse 30, NW I, 95440 Bayreuth, Germany*
[c] *Department of Chemistry, Macromolecular Chemistry I, Universität Bayreuth, Universitätsstrasse 30, NW I, 95440 Bayreuth, Germany*
[d] *Department of Chemistry, Macromolecular Chemistry II, Universität Bayreuth, Universitätsstrasse 30, NW I, 95440 Bayreuth, Germany*
[e] *Department of Chemistry, Physical Chemistry II, Universität Bayreuth, Universitätsstrasse 30, NW I, 95440 Bayreuth, Germany*

† Electronic supplementary information (ESI) available: Experimental section, powder X-ray diffraction data and single crystal X-ray diffraction data, Mössbauer spectra of 7–10 and magnetic measurements of 2, TGA and DSC measurements, POM micrographs of all complexes, AFM images of thin films of 7. CCDC 1835195, 1835196 and 1044903. For ESI and crystallographic data in CIF or other electronic format see DOI: 10.1039/c8tc05580g

transitions for complexes with short alkyl chains[27] and a more gradual SCO and crystal–liquid crystal phase transition for complexes with longer alkyl chains.[28] Further optimization of the system showed that a phase transition in meltable complexes can be used to control the spin transition.[29] Investigations of Albrecht *et al.* on amphiphilic iron(III) complexes in solution[30] and in the solid[31] revealed that an increase of the length of the alkyl chains did lead to higher cooperativity of the spin crossover due to an improved self-assembly. Furthermore, the combination of LC and SCO properties offers the opportunity of an orientation of the complexes *via* the electrical field. In the case of amphiphilic systems new strategies to process bulk SCO compounds into thin films also motivated such studies. Those could be obtained by techniques such as the Langmuir–Blodgett, spin coating, or drop casting.[21,30,32–34] Such self-assembled monolayers of SCO molecules as thin films can be studied by scanning tunneling microscopy (STM).[35] Self-assembling spin crossover complexes based on alkylated ligands reported so far are either based on mononuclear complexes (*e.g.* Langmuir–Blodgett film formation of the $[Fe(L_2)(NCS)_2]$ or $[Fe(L)_3]^{2+}$ $2NCS^-$ system with L = 2,2′-bipyridine substituted in position 4 and 4′ with long alkyl chains),[36,37] triazole-based coordination polymers with the triazole carrying alkyl trails (Langmuir–Blodgett film formation, solid state properties),[38–40] or complexes with amphiphilic counter ions (thin film formation).[41]

Please note that the SCO may be modified by the functionalization of ligands with long alkyl chains and by the processing, thus a prediction of the results so far is highly difficult.[37] However, for a purposeful synthesis of SCO-based materials, it is indispensable to be able to predict the impact of changes in the ligand structure on the SCO parameters.

For iron(II) complexes with amphiphilic Schiff base-like ligands used in our group, self-assembly behavior was observed but no LC properties.[42,43] The complexes crystallize in lipid layer like structures. In agreement with the results from Albrecht *et al.* longer alkyl chains support the formation of lipid layers and by this lead to improved spin crossover properties.[44] In one case an over 20 K wide thermal hysteresis loop is observed.[45] So far we were not able to investigate the PT properties of those complexes as they decompose at higher temperatures (above 350 K), a typical behavior for mono- and dinuclear complexes of this type. For the synthesis of more stable coordination polymers, relatively large bridging ligands as 1,2-bis(4-pyridyl)ethane (bpea), 1,2-bis(4-pyridyl)ethene (bpee), or 1,2-bis(4-pyridyl)ethyne (bpey) are necessary.[46,47] For the realization of those systems the self-assembly parameter (sap) needs to be considered, where interplay of the coordination number, the size of the axial ligands attached at the iron(II) center, and the alkyl chain length is summarized.[42] Through application of this parameter, we are now able to predict the successful synthesis of the coordination polymers with Schiff base-like ligand with 16–22 carbon atoms in the alkyl chain that crystallize in a lipid-layer like arrangement. Please note that despite of the number of examples it is still difficult for a given system to predict the packing of the molecules in the crystal and by this the spin crossover properties. Here we show that we are able to fine-tune the SCO parameters through control of the crystal packing – an essential point for future applications. Additionally, the investigation of amphiphilic SCO systems is one step further towards synthesis of self-assembled (mono-)layers of SCO molecules. In contrast to the coordination polymers with amphiphilic ligands reported so far, the system presented here compromised neutral polymer chains. The influence of this differences on the SCO properties and film formation will be discussed.

2. Results and discussion

2.1 Synthesis

In Scheme 1, the general structure of the ligands and complexes discussed in this work and the used abbreviations are given. The ligands $\mathbf{H_2L(}$***y*****+1)** were synthesized following procedures described in literature for similar systems.[44] The reaction with iron(II) acetate[48] in methanol yielded the corresponding parent complexes $\mathbf{[FeL(}$***y*****+1)(MeOH)**$\mathbf{_2]}$ with two methanol molecules as axial ligand. For $\mathbf{[FeL(20)(MeOH)_2]}$, single crystals of high enough quality were obtained to determine the crystal structure that is discussed in the following. In the next step the axial ligands (MeOH) were substituted by 1,2-bis(4-pyridyl)ethyne[49,50] (bpey), 1,2-bis(4-pyridyl)ethene (bpee), or 1,2-bis(4-pyridyl)ethane (bpea), respectively to yield complexes **1–6** (ESI,† Scheme S1). Single crystals of **4·tol** and **6·tol** were obtained by slow diffusion setups whose structures are also discussed in the following. All iron(II) complexes are very air sensitive in solution and in part also in the solid state. For comparison purpose, the corresponding oxidized μ-O-complexes **7–10** were synthesized as well.

2.2. X-ray structure analysis

Platelet-like crystals of $\mathbf{[FeL(20)(MeOH)_2]}$ and **4·tol** and spicular crystals of **6·tol** suitable for X-ray structure analysis were obtained either directly from the synthesis or by slow diffusion setups. The crystal data were collected at 133 K ($\mathbf{[FeL(20)(MeOH)_2]}$ and **4·tol**) and 200 K (**6·tol**) and are summarized in the ESI,† Table S1. For **4·tol** a non-mathematical twin was obtained. Therefore, the refinement of the crystal structure is incomplete and it will be discussed as a structural motif only. Thus, only the general packing of the molecules is considered but no exact bond lengths or angles are given. Please note that it is very difficult to obtain large enough single crystals of such amphiphilic complexes and that the molecular weight per iron center is with more than 1000 g mol^{-1} very high. Thus, the *R* values are in all cases larger than the ones usually obtained for smaller molecules. All complexes crystallized in the triclinic space group $P\bar{1}$. Selected bond lengths and angles within the first coordination sphere of the iron center are listed in Table 1. An ORTEP drawing of the asymmetric unit is given in Fig. 1.

The iron center of $\mathbf{[FeL(20)(MeOH)_2]}$ has an N_2O_4 coordination sphere build by the equatorial N_2O_2-coordinating Schiff base-like ligand and two axially coordinating methanol, as shown at the top of Fig. 1. The average bond lengths are 2.10 Å (Fe–N_{eq}), 2.00 Å (Fe–O_{eq}), and 2.19 Å (Fe–O_{ax}) and the

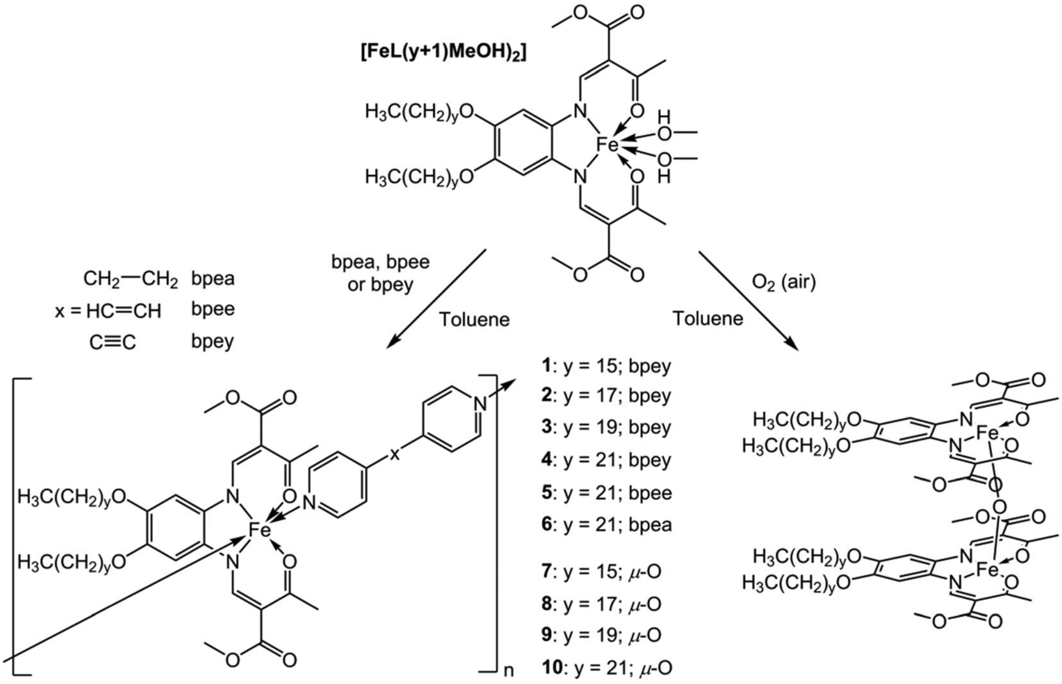

Scheme 1 General structure of the coordination polymers and the μ-O-complexes discussed in this work and their abbreviations. (y + 1) denotes to the number of carbon atoms of the alkyl chain, bpea, bpee, and bpey denote to the bridging ligands 1,2-bis(4-pyridyl)ethane, 1,2-bis(4-pyridyl)ethene and 1,2-bis(4-pyridyl)ethyne.

Table 1 Selected bond lengths [Å] and angles [°] of **[FeL(20)(MeOH)$_2$]***, **4·tol**, and **6·tol** within the first coordination sphere and their dimensions [Å] and sap[42]

Compound	Fe–N$_{eq}$	Fe–O$_{eq}$	Fe–O$_{ax}$/N$_{ax}$	O$_{eq}$–Fe–O$_{eq}$	L$_{ax}$–Fe–L$_{ax}$	∢L$_{ax}$[a]	α	β	*H*	*B*	*L*	sap
[FeL(20)(MeOH)$_2$]	2.097(4) 2.100(4)	1.990(4) 2.019(3)	2.199(4) 2.184(3)	109.38(14)	166.88(11)	—	162	176	8	15	33	0.7
4·tol	1.9 1.9	2.0 1.9	2.0 2.0	86	176	5	112	131	14	15	29	1.0
6·tol	1.885(4) 1.908(3)	1.917(3) 1.953(3)	2.012(3) 2.003(4)	90.05(10)	175.91(16)	88	140	158	13	14	29	0.9

[a] Torsion angle between the axial pyridine rings.

O–Fe–O angle is 109°. Those values are in the region typical for octahedral HS iron(II) complexes of this ligand type.[46,51–53] The L$_{ax}$–Fe–L$_{ax}$ angle of 166° deviates slightly of the expected 180° for a perfect octahedral coordination sphere. An analysis of the packing of the molecules in the crystal, given at the top of Fig. 2, reveals that they are ordered in a lipid layer-like arrangement. The alkyl chains build parallel layers with an approximate layer to layer distance of about 4.2 Å. This distance is typical for stabilizing van der Waals interactions (London Dispersion forces) between the alkyl chains and a similar behavior is observed for other amphiphilic complexes, not only for this general ligand type, but also for others that are less related.[42] The iron containing head groups are oriented to each other between the layers of the alkyl chains. Two intermolecular hydrogen bonds are observed within the layer of the head groups. The hydrogen bond O(9)–H(9)···O(3) connects the complex molecule in the same lipid-like layer to form infinite chains along [1 0 0] and O(10)–H(10A)···O(2) connects the head groups of two opposite layers through the formation of dimers. The details (distances and angles) of the hydrogen bonds are given in Table 2.

ORTEP drawings of the asymmetric unit of **4·tol** and **6·tol** are given in the center and at the bottom of Fig. 1. In both cases the iron center has an N$_4$O$_2$ coordination sphere build of the equatorial N$_2$O$_2$ coordinating ligand and the bridging N coordinating ligand. The average bond lengths within the first coordination sphere are 1.89 Å/1.90 Å (Fe–N$_{eq}$), 1.96 Å/1.94 Å (Fe–O$_{eq}$), and 1.99 Å/2.01 Å (Fe–N$_{ax}$), respectively. The O–Fe–O angles are 88° in average. Those values are in the region typical for LS iron(II) complexes of this ligand type.[50,54] The L$_{ax}$–Fe–L$_{ax}$ angle of 176° (**4·tol** and **6·tol**) deviates only slightly of the expected 180° for a perfect octahedral coordination sphere. The torsion angle between the axial pyridine rings is 5° for **4·tol** and 88° for **6·tol.** The remaining electron density of **6·tol** indicates included solvent molecules. However, due to a strong disorder, they could not be further refined and therefore SQUEEZE from PLATON[55] was used. A total number of 97 electrons were removed from the refinement with a void

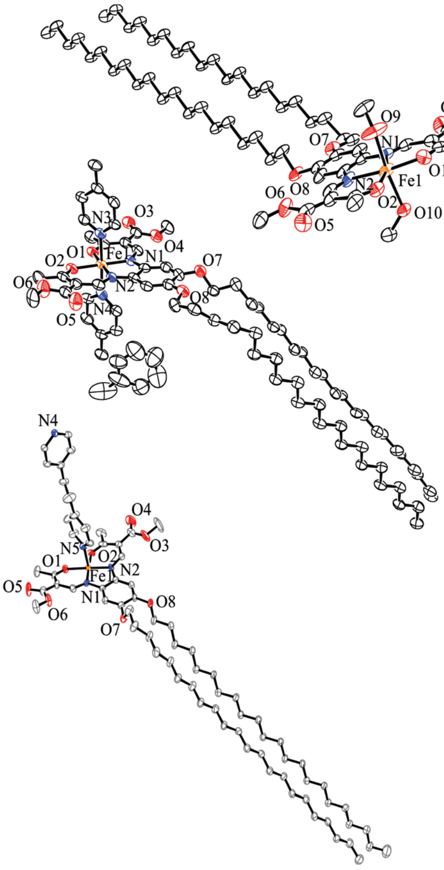

Fig. 1 ORTEP drawing of the asymmetric unit of the crystal structure of **[FeL(20)(MeOH)$_2$]** (top), **4·tol** (center) and **6·tol** (bottom). Hydrogen atoms are omitted for clarity. Thermal ellipsoids shown at the 50% probability level.

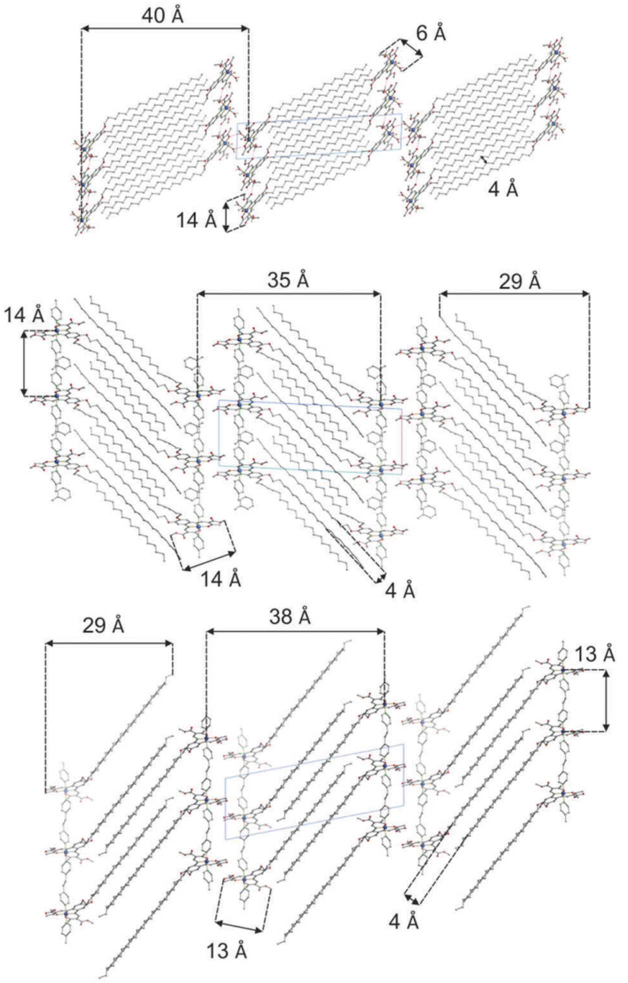

Fig. 2 Molecular packing of **[FeL(20)(MeOH)$_2$]** along [0.3 2.3 0] (top), **4·tol** along [1 0 0] (center) and **6·tol** along [1 0 0] (bottom) illustrating selected intermolecular distances discussed in the manuscript. Hydrogen atoms are omitted for clarity.

Table 2 Distances [Å] and angles [°] of the hydrogen bonds of **[FeL(20)(MeOH)$_2$]***

Bond	D–H	H···A	A···D	D–H···A
O(9)–H(9)···O(3)[a]	0.84	1.87	2.672(7)	161
O(10)–H(10A)···O(2)[b]	0.84	1.95	2.767(4)	165

[a] 1 + x, y, z. [b] 1 − x, 2 − y, 2 − z.

volume of 946 Å^3. Consequently, intermolecular contacts between the polar head groups cannot be discussed for both complexes.

The packing of the molecules in the crystal is for both complexes very similar to that of **[FeL(20)(MeOH)$_2$]**. The distances between the alkyl chains correspond to a maximum of stabilizing van der Waals interactions (approx. 4.2 Å), in good agreement with the particular high ordering of the alkyl chains without major bending. As shown in Fig. 2 (center and bottom), the molecules are ordered in the crystal in a lipid-layer like arrangement. One significant difference between the three structures are the angles between the plain of the chelate cycle and the alkyl chains. Here we can define two angles: the bending of the alkyl chains relative to the plane of the equatorial ligand (angle α) and the shift sideward in the plane of the chelate cycle (angle β). A schematic presentation of the angles is shown in Fig. 3. For **[FeL(20)(MeOH)$_2$]** the bending α is 162° and the shifting β is 176°. This bending and shifting is more pronounced for the two complexes **4·tol** and **6·tol** with the longer chains. The values for **4·tol** are α = 112° and β = 131° and for **6·tol** α = 140° and β = 158°, respectively. This deviation of an ideal linear arrangement along the equatorial ligand (both angles 180°) is responsible for the possibility of the complexes to crystallize in a hexa-coordinated fashion. The orientation compensates the sterical demand of the axial ligand and, therefore, provides a lipid layer-like ordering.

As discussed in a previous work,[42] there is a relation between the size of the head group (height H plus broadness B) and the length L of the molecule which is called sap (self-assembly parameter):

$$\text{sap} = \frac{(H + B)}{L}$$

A lipid layer-like arrangement can be expected for a sap ≈ 1. The calculated values for **[FeL(20)(MeOH)$_2$]**, **4·tol** and **6·tol** are

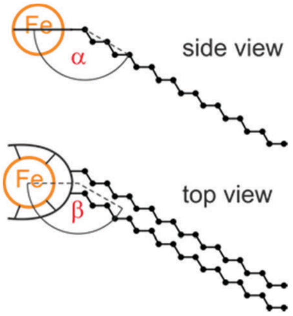

Fig. 3 Schematic representation of the angles for the bending α and shifting β between the plane of the chelate cycle and the alkyl chains.

shown in Table 1. **4·tol** and **6·tol** have a sap of around 1 which fits very well to the obtained lipid layer-like structure in the crystal packing. However, **[FeL(20)(MeOH)$_2$]** also shows this kind of arrangement despite of having a sap of 0.7. In literature, so far all examined complexes have values around 1 or higher, so it is possible that values below 1 can also lead to lipid layer-like structures. Another reason might be, that for **[FeL(20)(MeOH)$_2$]** the structure is additionally stabilized by the intermolecular hydrogen bond network. A similar behavior is observed for other methanol complexes of this ligand type with shorter alkyl chains.[44]

In order to analyze, if the fine crystalline samples of **1–6** assume similar structures, the calculated X-ray powder diffraction pattern of **4·tol** and **6·tol** are compared with the measured XRPD patterns of **1–6**. The results are given in Fig. 4. Indeed, in the region of 6°–8° 2θ and 20°–25° 2θ strong similarities in the diffraction patterns are observed. This can be used as first indication that in all cases coordination polymers were formed that assemble in a lipid layer like arrangement of the amphiphilic molecules with an approximate distance between the iron centers within the polymer chain of 13–14 Å and a distance between the layers of the alkyl chain in the region of 4.3 Å.[42,56] Especially for the coordination polymers **1–4** with bpey as bridging ligand strong similarities are observed thus a very similar packing of the molecules in the crystal is likely. For the more flexible ligands bpee and bpea, the obtained samples are less crystalline with slightly broader reflexes. However, the overall pattern is still very similar to that observed for **1–4** and to that of the calculated patterns from the single crystals. For comparison purpose, the XRPD spectra of the corresponding the μ-O-complexes **7–10** were recorded as well and are given in the ESI,† Fig. S1.

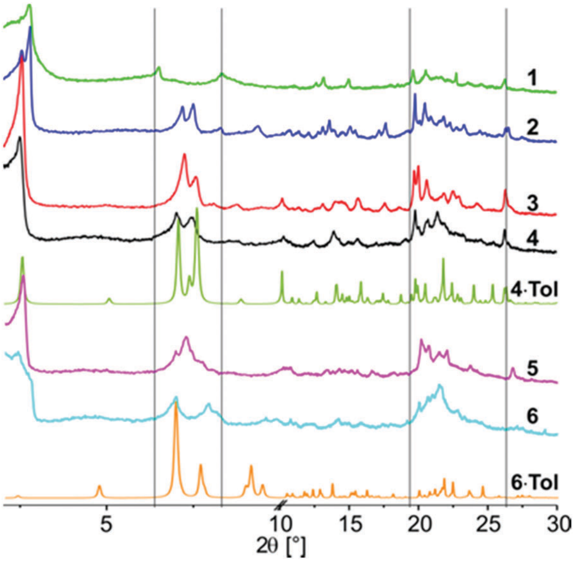

Fig. 4 XRPD spectra of **1–6** in the range of 2°–30° 2θ at room temperature and the calculated XRPD data of the single crystal of **4·tol** and **6·tol**. The vertical lines were included as guide for the eye.

In contrast to the XRPD spectra of **1–6**, for the μ-O-complexes **7–10** a set of reflexes is observed in the region of 3.5°–6.5° 2θ, whereas in the region 6.5°–8° 2θ no reflexes are observed. In the 20°–25° 2θ, on the other side, some reflexes are observed as in the case of the coordination polymers. For all samples strong reflexes are observed below 3.5° 2θ. In the case of the coordination polymers, the signal appears around 2.5° 2θ. By using Bragg's law ($n\lambda = 2d\sin\theta$; $n = 1$, $\lambda = 1.54184$ Å, d = interplanar distance, θ = scattering angle) the related distances can be calculated and correlated with distances observed in the crystal packing of **4·tol** and **6·tol** (Table 3 and Fig. 2). They fit very well to the Fe–Fe distance in the lipid layer-like structure. Furthermore, the trend for **1**, **3**, **4**, **5**, and **6** shows that the distance depends on the alkyl chain length which determines the thickness of the layer. Only **2** deviates slightly with two signals appearing, one a bit lower and one a bit higher than expected. It is possible that during the crystallization process two slightly different phases were formed. However, results from Mössbauer spectroscopy and magnetic measurements indicate that only one independent iron species is present.

2.3. Magnetic properties

Magnetic measurements were done for all coordination polymers (**1–6**), the results are displayed in Fig. 5 as plot of the HS fraction γ_{HS} *vs.* T. The $\chi_M T$ *vs.* T plot is shown in Fig. S2 (ESI†). At room temperature the complexes **1–5** are clearly diamagnetic with a $\chi_M T$ product in the range between 0.02 and 0.27 cm^3 K mol^{-1}. **6** undergoes already a partial spin transition at this temperature and has a $\chi_M T$ value of 0.89 cm^3 K mol^{-1}. The spin state is confirmed by room temperature Mössbauer spectroscopy, the details are summarized in Table 4. For the complexes **1–5** the average values determined at room temperature are

Table 3 XRPD data and the calculated interplanar distances of **1–6**

Compound	2θ [°]	d [Å]
1	2.750	32
2	2.525/2.765	35/32
3	2.540	35
4	2.465	36
4·tol	2.503[a]	35[a]
5	2.510	35
6	2.360	37
6·tol	2.316[a]	38[a]

[a] Calculated values from the single crystal X-ray structure using Mercury.[57]

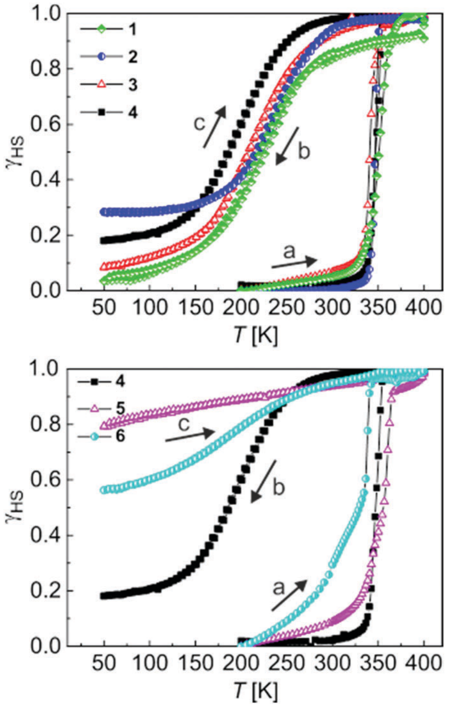

Fig. 5 Magnetic measurements of **1–4** (top) and **4–6** (bottom) with γ_{HS} plotted against T. Temperature sequence: first heating (a), cooling (b), second heating (c).

δ = 0.342 mm s^{-1} and ΔE_Q = 1.193 mm s^{-1}. Those are characteristic for a low spin Fe(II) in an octahedral N_4O_2 coordination sphere.[58–60] For complex **6**, on the other hand, two quadrupole split doublets are observed (Fig. 6 left, Table 4), of which one is characteristic for iron(II) in the low spin state, while the other one is characteristic for iron(II) in the HS state. Analysis of the relative area of the two doublets reveals a HS fraction of 0.17. Considering the differences of the Lamb–Mössbauer parameters for iron(II) in the HS and the LS state, this is in good agreement with the results from the magnetic measurement which show a γ_{HS} value of 0.26 at room temperature.

Upon heating to 400 K the complexes **1–4** with different alkyl chain lengths and bpey as bridging ligand show a very similar abrupt, irreversible SCO from LS to HS with $T_{1/2}$ of 354 K for **1**, 347 K for **2**, 340 K for **3** and 344/351 K for **4** (top of Fig. 5). The room temperature $\chi_M T$ product after annealing is with an average value of 2.79 cm^3 K mol^{-1} lower than expected for an iron(II) in the HS state (details see Table 4). This is most likely due to the phase transition observed by temperature dependent polarized optical microscopy and powder XRD. The now observed gradual SCO already starts around room temperature and by this leads to reduced $\chi_M T$ values. In order to confirm that a spin transition took place and to check if it is complete or not, Mössbauer spectra were recorded of the annealed (heating to 380 K for a few minutes) complexes at room temperature. Those measurements confirm that after the first heating the samples are in the HS state at room temperature (see Fig. 6 and Table 5). After heating to 380 K (above SCO temperature, but below the melting point, see below), for the complexes **3–6** a single HS site is observed. However, in the case of **1** and **2** a second doublet is observed whose parameters cannot be related to iron(II) in the HS or the LS state. Comparison with the room temperature Mössbauer parameters of the oxidized complexes **7–10** (ESI,† Fig. S3 and Table 4) confirms that this doublet belongs to a Fe(III) HS species. This indicates that the compound oxidized either during the heating process or during the Mössbauer measurement itself (around 5 days at room temperature). During the magnetic measurements in the SQUID magnetometer, no indications for the formation of oxidized species during the heating progress are observed. Here, subsequent cooling of the complexes

Table 4 Magnetic properties of **1–10**. The magnetic susceptibility data of **1–6** is summarized on the left side. $T_{1/2}$ is used for the first heating and $T_{1/2}$* is used for the following cooling/heating cycles after annealing. On the right side the room temperature ^{57}Fe Mössbauer data are summarized for **1–10**. The SCO coordination polymers **1–6** were measured before and after annealing

	Magnetic measurements					Mössbauer studies			
Compound	$\chi_M T$ (rt) [cm^3 K mol^{-1}]	γ_{HS} (rt)	γ_{HS} (50 K)	$T_{1/2}$ and $T_{1/2}$* [K]	Species	δ [mm s^{-1}]	ΔE_Q [mm s^{-1}]	$\Gamma/2$ [mm s^{-1}]	Area [%]
1	0.15	0.05	—	354	Fe(II) LS	0.338(5)	1.173(10)	0.163(7)	100
$\mathbf{1}_{\text{annealed}}$	2.58	0.86	0.04	225	Fe(II) HS	0.96(8)	2.11(16)	0.238(6)	69(14)
					Fe(III) HS	0.3(3)	0.8(6)	0.3(2)	31(14)
2	0.02	0.01	—	347	Fe(II) LS	0.331(4)	1.175(8)	0.160(6)	100
$\mathbf{2}_{\text{annealed}}$	2.83	0.94	0.28	238	Fe(II) HS	0.936(18)	2.21(4)	0.18(3)	77(8)
					Fe(III) HS	0.35(9)	0.81(17)	0.22(12)	22(8)
3	0.21	0.07	—	340	Fe(II) LS	0.343(2)	1.203(3)	0.142(2)	100
$\mathbf{3}_{\text{annealed}}$	2.79	0.92	0.08	216	Fe(II) HS	0.924(4)	2.181(8)	0.158(6)	100
4	0.07	0.02	—	344/351	Fe(II) LS	0.345(4)	1.206(8)	0.141(6)	100
$\mathbf{4}_{\text{annealed}}$	2.94	0.98	0.18	199	Fe(II) HS	0.951(12)	2.14(3)	0.178(19)	100
5	0.27	0.09	—	340/369	Fe(II) LS	0.355(3)	1.207(5)	0.155(4)	100
$\mathbf{5}_{\text{annealed}}$	2.82	0.94	0.79	—	Fe(II) HS	0.879(7)	2.220(14)	0.178(11)	100
6	0.89	0.26	—	338	Fe(II) LS	0.389(17)	1.10(3)	0.231(14)	83(4)
					Fe(II) HS	0.90(7)	2.24(17)	0.21(6)	17(4)
$\mathbf{6}_{\text{annealed}}$	2.85	0.95	0.56	199	Fe(II) HS	0.94(3)	2.23(6)	0.19(5)	100
7	—	—	—	—	Fe(III) HS	0.334(16)	0.77(3)	0.17(2)	100
8	—	—	—	—	Fe(III) HS	0.335(13)	0.74(2)	0.200(18)	100
9	—	—	—	—	Fe(III) HS	0.330(16)	0.75(3)	0.18(2)	100
10	—	—	—	—	Fe(III) HS	0.31(4)	0.73(6)	0.23(5)	100

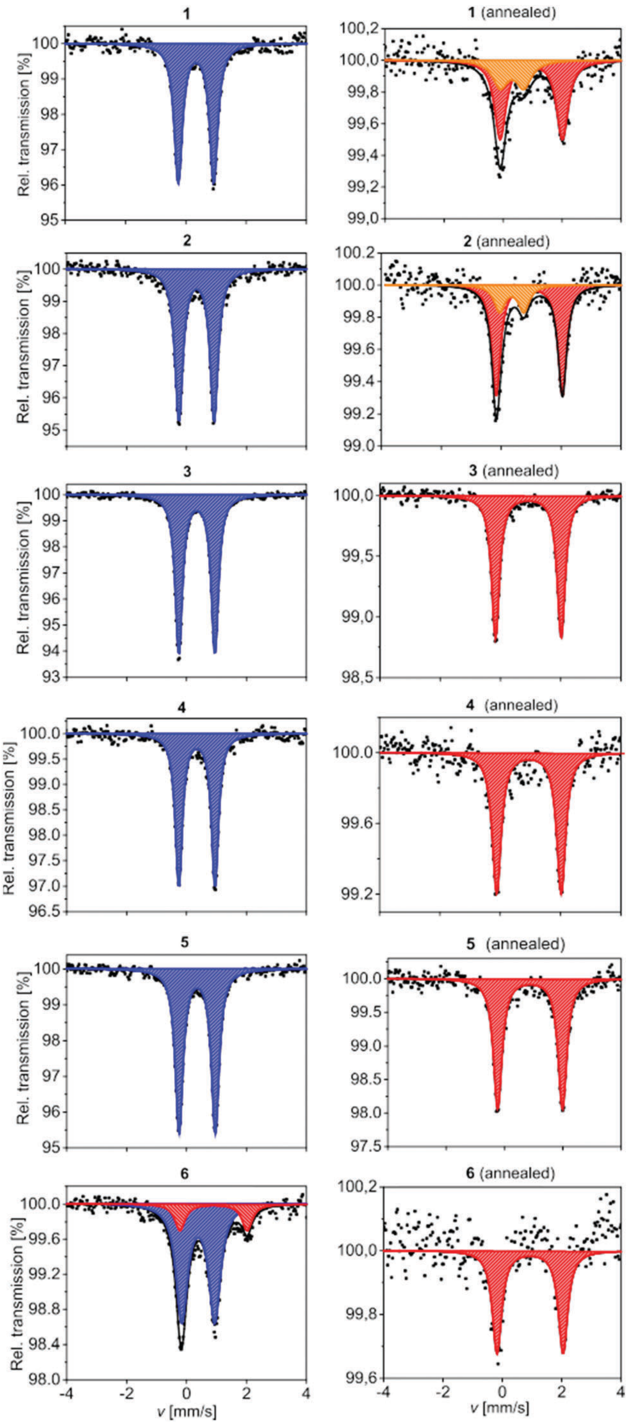

Fig. 6 Mössbauer spectra of **1–6** measured at room temperature (left: before annealing, right: after annealing at 380 K for about 10 min). The blue doublet corresponds to iron(II) in the low spin state and the read doublet corresponds to iron(II) in the high spin state. The orange doublet is characteristic for the corresponding μ-O-iron(III) species (high spin state). The corresponding parameters are summarized in Table 4.

to 50 K reveals a gradual, reversible SCO from HS to LS for all complexes with $T_{1/2}$* values of 225 K for **1**, 238 K for **2**, 216 K for **3**, and 199 K for **4**. This SCO is incomplete and at 50 K γ_{HS} varies between 0.04 for **1**, 0.28 for **2**, 0.08 for **3**, and 0.18 for **4**, respectively.

For **4–6** the alkyl chain length of C22 was kept constant, but the axial ligand was varied from bpey, to bpee and bpea. At the bottom of Fig. 5 the results from the temperature dependent measurement are given that show that the influence of the bridging ligand on the SCO behavior is stronger in comparison to a change of the alkyl chain length. This is due to stronger interactions of the iron center with the bridging ligand than with the alkyl chains at the outer periphery. From bpey (**4**) to bpee (**5**) and bpea (**6**) the SCO of the first heating becomes more and more gradual. This can be explained with the decreasing rigidity of the bridging ligand. A more rigid system tends to have a more abrupt SCO. $T_{1/2}$ of the abrupt part of the SCO is 344/351 K for **4**, 340/369 K for **5**, and 338 K for **6**. Upon cooling to 50 K, the second SCO is incomplete for bpey (**4**) and bpea (**6**) with a γ_{HS} fraction of 0.18 and 0.56, respectively, and almost disappears for bpee (**5**) with a γ_{HS} fraction of 0.79. In order to analyze the spin crossover and potential phase transition behavior in more detail, the magnetic measurements were repeated for **2** using slightly varied conditions. The sample was heated up to 354 K (only slightly above $T_{1/2}$ and significantly below any further phase transitions, see TGA/DSC) with three repeating heating and cooling cycles (Fig. S4, ESI†). Independent of this, the same initial abrupt SCO is observed followed by a gradual SCO during the subsequent cooling and heating cycles. Thus, the SCO behavior is not influenced by any subsequent phase transitions/melting of the sample above 354 K. When **2** is measured for three heating and cooling cycles it can be seen that at 50 K γ_{HS} increases after each cycle from 0.30 to 0.56 to 0.76 and the gradual SCO is slowly disappearing.

2.4. TGA and DSC

In both single crystal X-ray structures of **4·tol** and **6·tol** solvent molecules were observed in the crystal packing. From the literature it is known that SCO phenomena can be triggered or influenced by a solvent loss.[61,62] Consequently, TGA measurements of the fine crystalline samples **1–6** were performed to analyze if solvent is included in the crystal packing that could influence the SCO behavior and explain the differences between the first and all subsequent heating modes. Please note that the complexes were dried in vacuum for several hours prior to all characterization to remove as much solvent as possible to reduce such effects. The results of the TGA measurements are displayed in the ESI,† Fig. S5. In the case of **2**, **3**, **5** and **6**, the TGA shows a small step around the SCO temperature which can be associated with some solvent loss. On the other side, for the complexes **1** and **4** no indications for the presence of additional solvent in the sample is observed (ESI,† Table S2). The temperature range and percentage of the weight loss corresponds best to the inclusion of 0.5 to 1 methanol molecules per repeating unit of the coordination polymer (probably from the starting material). However, according to elemental analysis, the inclusion of toluene is more likely. As the magnetic properties of all SCO coordination polymers is similar independent of the presence or absence of included solvent molecules, an influence of the solvent molecules can be ruled out. An irreversible phase transition accompanying the

Table 5 Spin-crossover temperature $T_{1/2}$ obtained from magnetic measurements and thermodynamic parameters calculated from DSC for **1–6**

Compound	SCO $T_{1/2}$ [K]	DSC $T_{\max}$ [K]	ΔH [kJ mol^{-1}]	ΔS [J K^{-1} mol^{-1}]
1	354	354	30.15	84.26
2	347	351	45.18	125.19
3	340	351	69.57	213.49
4	344/351	353	78.83	237.57
5	340/369	336/362	73.24	203.33
6	338	340	67.85	197.32

spin transition could be another reason for the different SCO properties for the first heating and all subsequent cycles. In order to analyse this, DSC measurements were performed with two heating and cooling cycles. The results are summarized in the ESI,† Fig. S6 and in Table 5. While there are no differences between the first and the second cooling cycle, in the heating mode pronounced differences between the first and the second cycle are observed. For the first heating, each coordination polymer undergoes an endothermic process around the $T_{1/2}$ of the SCO, as illustrated in Fig. 7. The calculated enthalpy (ΔH) and entropy (ΔS) changes exceed by far the expected values for an iron(II) SCO (ΔH = 10 kJ mol^{-1} and ΔS = 40 J K^{-1} mol^{-1}, Table 5).[1,2,63] This points towards a phase transition taking place during the spin transition. Either the spin crossover triggers the phase transition or *vice versa*. The absolute values of ΔH and ΔS strongly depend on the chain length of the equatorial ligand and increase with the extension of the alkyl chain (**1–4**). Thus, the spin transition is most likely triggered by a phase transition related to those alkyl chains. Furthermore, the values of ΔH and ΔS increase by decreasing flexibility of the bridging ligand (**4–6**) (Fig. 8), however, here the changes are not as pronounced. The evaporation of additional solvent molecules also has an influence on ΔH and ΔS. However, in our case the influence is too small to be observable as only the number of C atoms appears to be relevant for the correlation shown in Fig. 8. The two cooling cycles and the second heating cycle confirm the assumption that additional phase transitions take place next to the spin transition. The related structural changes were investigated further using temperature dependent powder XRD.

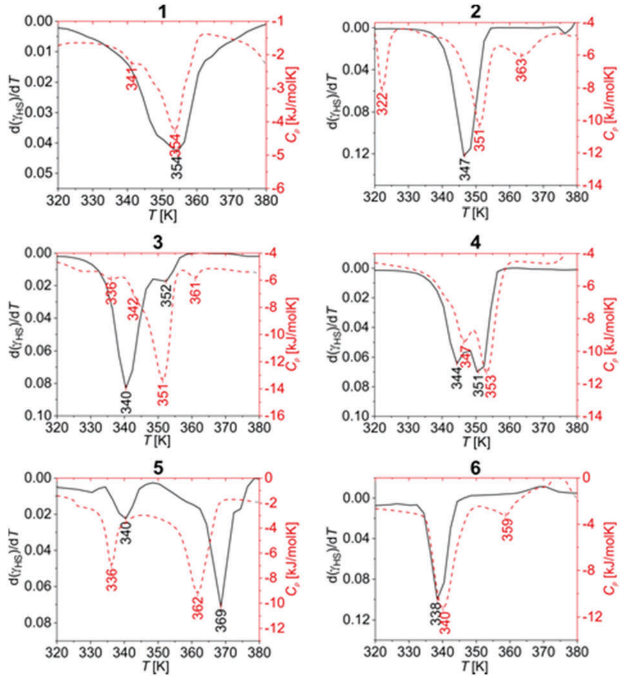

Fig. 7 DSC measurements (red, dashed line) and the first derivative of the magnetic measurements (black, solid line) of **1–6** in the temperature range between 320 and 380 K illustrating a good agreement between both methods. The slight difference between the temperatures is most likely due to the different measurement velocities of the two methods.

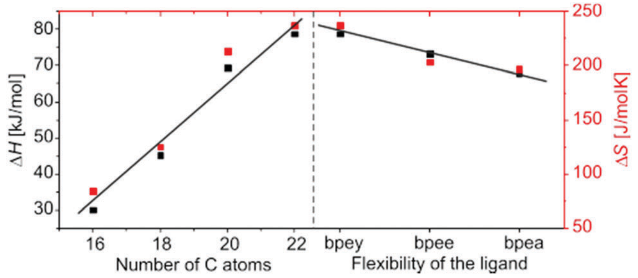

Fig. 8 Influence of the chain length and of the flexibility of the bridging ligand on the enthalpy ΔH and entropy ΔS.

Temperature dependent XRPD measurements were carried out to analyze the structural changes associated to the combined spin and phase transition. Those will be reflected in changes in the XRPD patterns and can be related to characteristic Fe–Fe distances in the crystal packing (*e.g.* between the layers or interchain). Please note that the XRPD measurements mentioned in the previous paragraph were measured in a capillary, whereas the temperature dependent XRPD measurements were measured on a flat plate. Thus, small differences in the 2θ values between those two methods can occur. In Fig. 9, the temperature dependent changes in the 2.0–3.5 2θ region is displayed for the complexes **2**, **4** and **5** as typical examples. The corresponding powder diffraction patterns of the other three complexes together with the diffraction patterns in the whole 2θ range are given in the ESI,† Fig. S7 and S8. As already discussed in the X-ray structure analysis section and illustrated in Table 3, the 2.0–3.5 2θ region is characteristic for the distance between the layers of the lipid-like structure. Upon heating of **4**, three different phases are observed. Starting at

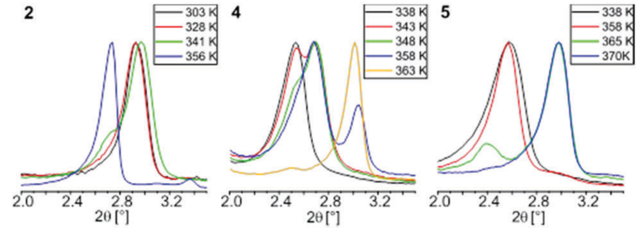

Fig. 9 Temperature dependent XRPD spectra of **2**, **4** and **5** displayed in the 2.0°–3.5° 2θ range. The temperatures were selected based on the DSC measurements and the phase transitions observed therein.

room temperature upon heating to 338 K a first phase with a peak maximum at 2.5° 2θ is observed. At 343 K a second peak appears at 2.7° 2θ, that increases in intensity at 348 K while the intensity of the first peak decreases. At 358 K the first peak disappeared completely and a third peak starts to appear at 3.0° 2θ. At 363 K this is the only peak. The increase in the 2θ values upon increasing temperature corresponds to a decrease of the distances between the layers, thus a rearrangement of the alkyl chains of the complexes takes place. The other complexes show similar phase transitions with either two (**2** and **5**) or three (**1**, **3**, **4**, and **6**) different phases. No systematic trend can be observed if the peak maximum shifts to higher (**4** and **5**) or lower (**2** and **6**) 2θ values. In the case of **3** the intermediate phase at 363 K is shifted to higher 2θ values and upon further heating it goes back to almost the original value, whereas for **1** an opposite trend is observed with the highest temperature peak in the middle between the two others. Thus the statement that can be derived from those results is that the phase transition is accompanied by an irreversible rearrangement of the alkyl chains leading to changes in the distances between the polymer chains. Those changes are always in the 2.4–2.9 2θ region corresponding to distance changes in the range between 36.8 to 30.5 Å. The numbers indicate that this involves a significant structural re-organization that leads to a loss of cooperativity (and crystallinity) and a gradual SCO is observed afterwards. Those significant rearrangements also lead to a shift of peaks in the other 2θ regions, as illustrated in the ESI,† Fig. S8. In order to analyze the irreversible nature of this rearrangement in more detail, in the case of **1** two subsequent heating and cooling cycles were investigated. In the ESI,† Fig. S9, the room temperature XRD pattern before annealing (1st cycle), after heating to 413 K (2nd cycle) and after heating to 373 K (3rd cycle) are given. It can be seen that after the first heating the XRPD pattern did change, however no further changes are observed for subsequent heating cycles.

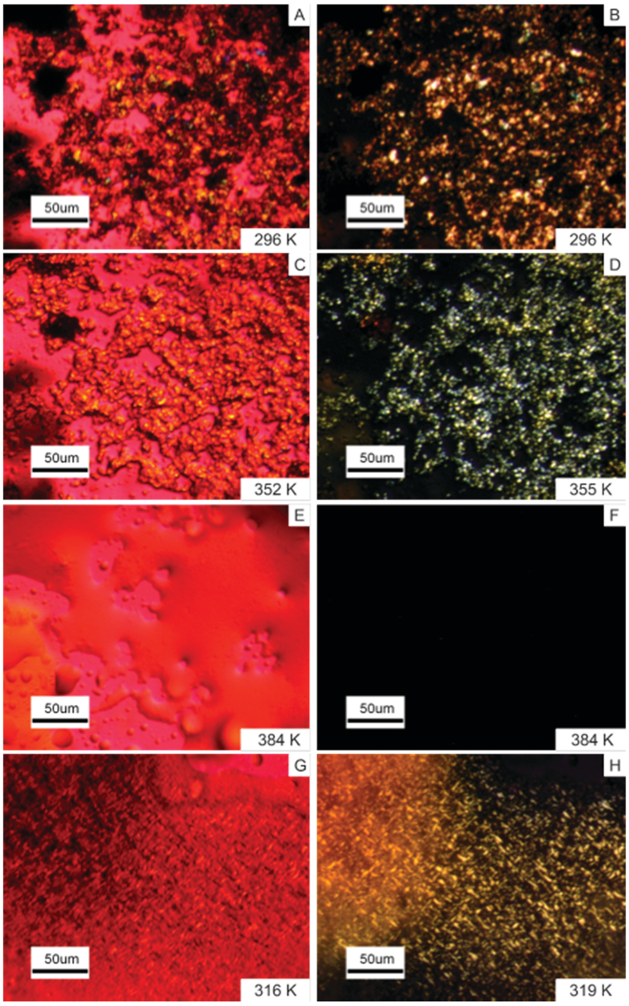

Fig. 10 POM micrographs of **4**. All images were taken under crossed polarized light. Left: With retardation plate, right: without retardation plate. (A and B) Crystalline powder from synthesis; (C and D) after combined SCO and phase transition; (E and F) melted sample; (G and H) formation of birefringent domains after cooling down.

2.5. Polarized optical microscopy

In order to analyze the phase transitions observed by DSC and XRPD in more detail, polarized optical microscopy (POM) pictures of all coordination polymers (**1–6**) were taken at different temperatures in the heating and cooling mode. The micrographs were recorded with and without a retardation plate (first order). In Fig. 10, the different phases of **4** as function of temperature are shown as typical example. In Fig. 10A and B the crystalline phase at room temperature is shown. Upon heating above the SCO temperature (Fig. 10C and D), the solid–solid phase transition detected by DSC measurements is reflected in changes in the POM micrograph. Further heating resulted in a melting of the sample around 384 K (Fig. 10E and F), in line with the outcomes of the DSC measurements. When the sample is cooled down after the initial melting, the formation of ordered, birefringent domains is observed (Fig. 10G and H). Thus, from the melt the complex crystallizes in a different phase compared to the crystallization from solution. This is in good agreement with the differences in the magnetic properties after the first heating and for all subsequent heatings. For the samples **1–3**, **5** and **6** a similar behavior is observed that is illustrated in the ESI,† Fig. S10–S14. In all cases the phase transition associated to the spin transition is reflected in changes of the POM micrographs. A chain length dependent difference is observed for the final structures. For the complexes **1**, **2**, and **3** with C16–C20 alkyl chains, spherulites are observed after cooling down from the melt, while for the complexes **4–6** with 22 carbon atoms in the alkyl chain, birefringent domains are observed after cooling. The corresponding POM micrographs are summarized in Fig. 11. The changes of the crystalline phase after heating to 400 K were additionally investigated using scanning electron microscopy for complex **4**. The results are shown in the ESI,† Fig. S15. After crystallization from solution, the sample consists of plate-like crystals with a thickness of about 65 nm. After heating and crystallization from the melt, again plate-like crystals are observed with a similar average thickness (82 nm).

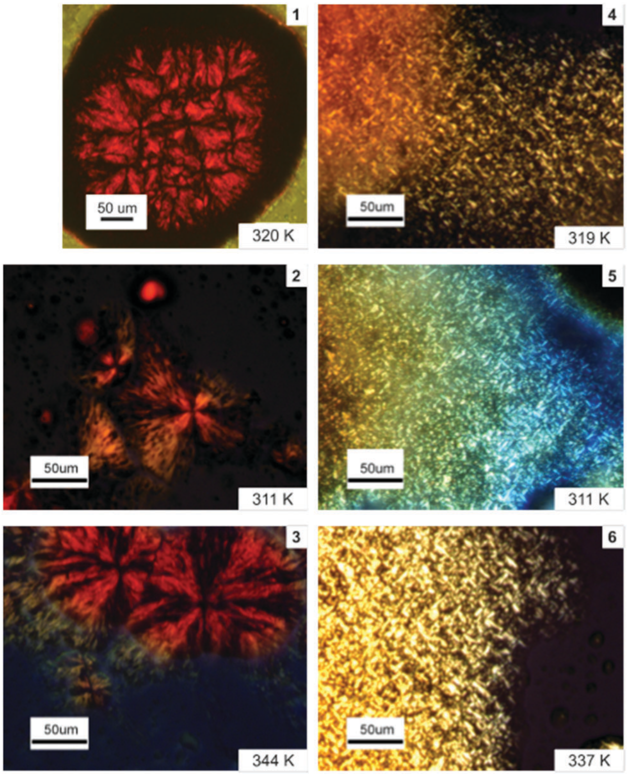

Fig. 11 POM micrographs with cross shaped spherulites of **1–3** and the birefringent domains of **4–6** after the first heating.

2.6. Processing as thin films

One of the advantages of amphiphilic complexes is that they offer an easy approach towards thin film formation. This is of importance for potential applications and the construction of functional devices. Consequently, the suitability of the complexes described in this work for film formation was tested using the spin coating approach. Due to the air sensitivity of the iron(II) complexes **1–6**, the corresponding μ-O-complex **7** was used for first preliminary investigations on the general suitability of these complexes for spin coating experiments. **7** was dissolved in toluene and spin coated with different concentrations and spin coating speeds on silicon wafers (Table 6). Spin coating on glass slides and ODTS functionalized silicon wafers was also tested, but did not result in a homogeneous film and is therefore not further discussed. The morphology of the films was then analyzed by atomic force microscopy (AFM) in tapping mode (Fig. S16, ESI†). Images with a resolution of 20 × 20 μm and 1 × 1 μm or 10 × 10 μm were recorded. To be able to measure the film thickness a small scratch was carved in the film with a needle. Due to this some of the removed material was deposited next to the edge and will be disregarded. Height profiles at different locations of the film were extracted and the film thickness and the RMS (root mean square) roughness was determined. With a concentration of 0.2 mg mL^{-1} (Fig. S16(A1), ESI†) no film formation can be observed. However, a network is formed with bridges of about 2 nm height. By increasing the concentration to 1.0 mg mL^{-1} a film with cavities is formed. The film thickness is 4 nm (Fig. S16(B2), ESI†) and the film RMS roughness is 1.4 nm (Fig. S16(B1), ESI†). A concentration of 5 mg mL^{-1} increases the film thickness up to 22 nm (Fig. S16(C2), ESI†) while the number of cavities decreases (Fig. S16(C1), ESI†). The cavities still reach down to the surface of the silicon wafer. Thus, the RMS roughness increases to 4.8 nm. By further increasing the concentration to 10 mg mL^{-1} the film thickness increases up to 30 nm (Fig. S16(D2), ESI†). At this concentration the cavities don't reach the silicon wafer anymore and the RMS roughness is decreased to 1.3 nm. The film becomes more and more homogenous (Fig. S16(D1), ESI†). For a concentration of 10 mg mL^{-1} the influence of the spin speed was investigated, too. An increase from 2000 rpm to 5000 rpm still resulted in the formation of a thin film with a thickness of 15 nm (Fig. S16(E2), ESI†) and an RMS roughness of 1.2 nm (Fig. S16(E1), ESI†).

Table 6 Spin coating parameters and film properties of **7**

Concentration [mg mL^{-1}]	Spin speed [rpm]	Average film thickness [nm]	RMS roughness [nm] (image)
0.2	2000	—	1.5 (A1)
1.0	2000	4	1.4 (B1)
5.0	2000	22	4.8 (C1)
10.0	2000	30	1.3 (D1)
10.0	5000	15	1.2 (E1)

Motivated by those results in the following the iron(II) spin crossover complex **4** was characterized with regard to film formation. TEM samples of **4** were prepared to analyze if the same behavior is observed as for the iron(III)-μ-O-complex and to investigate the structure of the film in more detail. Furthermore, the complex was dissolved in toluene or suspended in iso-octane to investigate the impact of the solvent on the film formation. The results are illustrated in Fig. 12. An incomplete film formation with gaps between the patterns was observed for the sample of **4** from toluene. The results are similar to those obtained for the AFM measurements done with **7** with low concentrations (Fig. S16(A1 and B1), ESI†). It appears that a similar film formation behavior is observed for both, the coordination polymer and the dimeric iron(III) complex if toluene is used as solvent. As **4** was insoluble in iso-octane the suspension was vortexed and ultrasonicated for some minutes. In the corresponding TEM pictures thin platelets and agglomerates of thin platelets are observed. In comparison

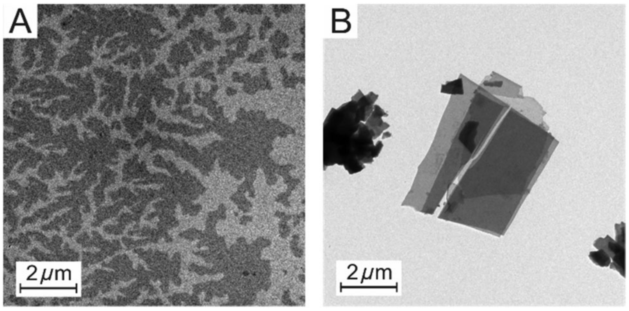

Fig. 12 TEM images of **4** prepared in toluene (A) and iso-octane (B).

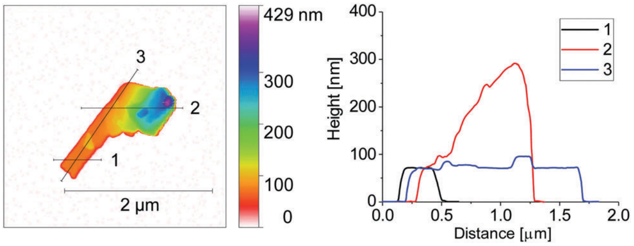

Fig. 13 AFM images of **4** prepared in iso-octane with the corresponding height profiles.

to the SEM measurements (Fig. S15, ESI†) done for the same complex before and after annealing at 400 K, the platelets appear to be much thinner and separated layers can be identified as seen in Fig. 12B. It is possible that the ultrasonication procedure in the unpolar solvent triggered a delamination of the layer-structure observed in the single crystal XRD. For the dried TEM sample the formation of agglomerates of the thin plates, as seen on the left side in Fig. 12B, was observed, too. To determine the thickness of the platelets AFM measurements of **4** dispersed in iso-octane were conducted. The results are illustrated in Fig. 13 and further images are given in the ESI,† Fig. S17. The images show again small agglomerates where the platelets are not perfectly stacked above each other but are piled up in a random way. This can be seen in the height profiles as some slopes are increasing constantly while others increase step-wise. The thickness of the platelets is roughly between 75 nm (Fig. S17(C), ESI†) and 260 nm (Fig. S17(A), ESI†). However, for the height of 260 nm it was difficult to distinguish between multistacking and thicker platelets. Please note that for the un-treated sample the SEM images (Fig. S15, ESI†) do not reveal such very thin platelets and the crystallites appear to be thicker.

3. Conclusion

In this manuscript the synthesis of six new iron(II) coordination polymers (**1–6**) with amphiphilic ligands is reported. All of them show an abrupt SCO above room temperature. After initial heating, **1–5** show a gradual and incomplete SCO at lower temperatures, while **6** remains in the HS state. The spin state before and after the first heating was confirmed by room temperature Mössbauer spectroscopy. DSC measurements of the six complexes reveal ΔH and ΔS values around the SCO temperature which are too high to be only associated with a spin transition. In addition, ΔH and ΔS increases with increasing alkyl chain length. This indicates the occurrence of a second process, namely a phase transition that is coupled to the spin transition and depends on the alkyl chain length and by this on the crystal packing. Single crystal X-ray structure analysis of three complexes (**[FeL(20)(MeOH)$_2$]**, **4·tol** and **6·tol**) reveals a lipid layer-like packing of the complexes in the crystal. The very similar PXRD patterns of all six coordination polymers indicates a similar packing in all cases that is dominated by the van der Waals interactions between the alkyl chains. Thus, by ligand design it is possible to predict the packing of the molecules in the crystal. The Fe–Fe distance between the layers depends on the length of the alkyl chains. Temperature dependent XRPD supports the assumption that the spin transition is coupled to a phase transition which is triggered by a rearrangement of the alkyl chains. This rearrangement is also observable in POM micrographs and in addition to that ordered, birefringent domains appear in the solid phase after the melting process. The film formation behavior was tested for complex **7** using spin coating. By increasing the concentration from 0.2 mg mL^{-1} to 10 mg mL^{-1} the properties of the film significantly improved and with 10 mg mL^{-1} a homogenous film with a thickness of 30 nm and a RMS roughness of 1.3 nm was formed. As expected, an increase of the spin speed resulted in a reduction of the film thickness. Preliminary TEM and AFM measurements were done on films and delaminated crystalline layers of the coordination polymer **4**. Further studies on the film *vs.* platelet formation and the corresponding magnetic properties are in progress.

Conflicts of interest

There are no conflicts to declare.

Acknowledgements

Financial support of the University of Bayreuth and the German Science formation (WE 3546/5-1 and SFB 840) is gratefully acknowledged. L. Peng, P. Pineda, J. Kronawitt and K. Küspert (MC, University of Bayreuth) are thanked for help with the calorimetric measurement and the polarized optical microscopy. We thank P. Mayer (University of Munich) for the collection of single crystal XRD data of **6·tol**.

References

1 *Spin-Crossover Materials*, ed. M. A. Halcrow, John Wiley & Sons Ltd, Chichester, 2013.
2 *Spin Crossover in Transition Metal Compounds I–III*, ed. P. Gütlich and H. A. Goodwin, Springer Berlin/Heidelberg, 2004, 233–235.
3 P. Gütlich, A. B. Gaspar and Y. Garcia, Spin state switching in iron coordination compounds, *Beilstein J. Org. Chem.*, 2013, **9**, 342–391.
4 J. Linares, E. Codjovi and Y. Garcia, Pressure and Temperature Spin Crossover Sensors with Optical Detection, *Sensors*, 2012, **12**, 4479–4492.
5 O. Kahn, C. Jay, J. Krober, R. Claude and F. Groliere, *Spin transition chemical compounds, and devices comprising read-, memory-, and erase-units, active medium which contains at least one of those compounds*, EP0666561, 1995.
6 O. Kahn, Spin-Transition Polymers: From Molecular Materials Toward Memory Devices, *Science*, 1998, **279**, 44–48.
7 J.-F. Létard, P. Guionneau and L. Goux-Capes, in *Spin Crossover in Transition Metal Compounds I–III*, ed. P. Gütlich and

H. A. Goodwin, Springer Berlin/Heidelberg, 2004, pp. 221–249.

8 A. Galet, A. B. Gaspar, M. C. Muñoz, G. V. Bukin, G. Levchenko and J. A. Real, Tunable Bistability in a Three-Dimensional Spin-Crossover Sensory- and Memory-Functional Material, *Adv. Mater.*, 2005, **17**, 2949–2953.

9 C. D. S. Brites, P. P. Lima, N. J. O. Silva, A. Millan, V. S. Amaral, F. Palacio and L. D. Carlos, Thermometry at the nanoscale, *Nanoscale*, 2012, **4**, 4799–4829.

10 O. Kraieva, C. M. Quintero, I. Suleimanov, E. M. Hernandez, D. Lagrange, L. Salmon, W. Nicolazzi, G. Molnar, C. Bergaud and A. Bousseksou, High Spatial Resolution Imaging of Transient Thermal Events Using Materials with Thermal Memory, *Small*, 2016, **12**, 6325–6331.

11 L. Salmon, G. Molnár, D. Zitouni, C. Quintero, C. Bergaud, J.-C. Micheau and A. Bousseksou, A novel approach for fluorescent thermometry and thermal imaging purposes using spin crossover nanoparticles, *J. Mater. Chem.*, 2010, **20**, 5499.

12 S. Cobo, G. Molnár, J. A. Real and A. Bousseksou, Multilayer Sequential Assembly of Thin Films That Display Room-Temperature Spin Crossover with Hysteresis, *Angew. Chem., Int. Ed.*, 2006, **45**, 5786–5789.

13 E. Coronado, J. R. Galán-Mascarós, M. Monrabal-Capilla, J. García-Martínez and P. Pardo-Ibáñez, Bistable Spin-Crossover Nanoparticles Showing Magnetic Thermal Hysteresis near Room Temperature, *Adv. Mater.*, 2007, **19**, 1359–1361.

14 J. Larionova, L. Salmon, Y. Guari, A. Tokarev, K. Molvinger, G. Molnár and A. Bousseksou, Towards the Ultimate Size Limit of the Memory Effect in Spin-Crossover Solids, *Angew. Chem., Int. Ed.*, 2008, **47**, 8236–8240.

15 M. Cavallini, I. Bergenti, S. Milita, G. Ruani, I. Salitros, Z.-R. Qu, R. Chandrasekar and M. Ruben, Micro- and Nano-patterning of Spin-Transition Compounds into Logical Structures, *Angew. Chem., Int. Ed.*, 2008, **47**, 8596–8600.

16 A. D. Naik, L. Stappers, J. Snauwaert, J. Fransaer and Y. Garcia, A Biomembrane Stencil for Crystal Growth and Soft Lithography of a Thermochromic Molecular Sensor, *Small*, 2010, **6**, 2842–2846.

17 Y. Raza, F. Volatron, S. Moldovan, O. Ersen, V. Huc, C. Martini, F. Brisset, A. Gloter, O. Stephan, A. Bousseksou, L. Catala and T. Mallah, Matrix-dependent cooperativity in spin crossover Fe(pyrazine)Pt$(CN)_4$ nanoparticles, *Chem. Commun.*, 2011, **47**, 11501–11503.

18 A. B. Gaspar, M. Seredyuk and P. Gütlich, Spin crossover in metallomesogens, *Coord. Chem. Rev.*, 2009, **253**, 2399–2413.

19 A. B. Gaspar and M. Seredyuk, Spin crossover in soft matter, *Coord. Chem. Rev.*, 2014, **268**, 41–58.

20 A. B. Gaspar and B. Weber, in *Molecular Magnetic Materials*, ed. B. Sieklucka and D. Pinkowicz, Wiley-VCH Verlag GmbH & Co. KGaA, Weinheim, Germany, 2017, pp. 231–252.

21 Y. Bodenthin, G. Schwarz, Z. Tomkowicz, M. Lommel, T. Geue, W. Haase, H. Möhwald, U. Pietsch and D. G. Kurth, Spin-crossover phenomena in extended multi-component metallo-supramolecular assemblies, *Coord. Chem. Rev.*, 2009, **253**, 2414–2422.

22 S. Hayami, in *Spin-Crossover Materials*, ed. M. A. Halcrow, John Wiley & Sons Ltd, Chichester, 2013, pp. 321–345.

23 H. S. Scott, B. Moubaraki, N. Paradis, G. Chastanet, J.-F. Letard, S. R. Batten and K. S. Murray, 2,2′-Dipyridylamino-based ligands with substituted alkyl chain groups and their mononuclear-M(II) spin crossover complexes, *J. Mater. Chem. C*, 2015, **3**, 7845–7857.

24 M. Seredyuk, A. B. Gaspar, V. Ksenofontov, Y. Galyametdinov, J. Kusz and P. Gütlich, Does the Solid–Liquid Crystal Phase Transition Provoke the Spin-State Change in Spin-Crossover Metallomesogens?, *J. Am. Chem. Soc.*, 2008, **130**, 1431–1439.

25 M. Seredyuk, A. B. Gaspar, V. Ksenofontov, Y. Galyametdinov, J. Kusz and P. Gütlich, Iron(II) Metallomesogens Exhibiting Coupled Spin State and Liquid Crystal Phase Transitions near Room Temperature, *Adv. Funct. Mater.*, 2008, **18**, 2089–2101.

26 S. Hayami, Y. Shigeyoshi, M. Akita, K. Inoue, K. Kato, K. Osaka, M. Takata, R. Kawajiri, T. Mitani and Y. Maeda, Reverse Spin Transition Triggered by a Structural Phase Transition, *Angew. Chem., Int. Ed.*, 2005, **44**, 4899–4903.

27 K. Senthil Kumar and M. Ruben, Emerging trends in spin crossover (SCO) based functional materials and devices, *Coord. Chem. Rev.*, 2017, **346**, 176–205.

28 M. Seredyuk, M. C. Munoz, V. Ksenofontov, P. Gutlich, Y. Galyametdinov and J. A. Real, Spin Crossover Star-Shaped Metallomesogens of Iron(II), *Inorg. Chem.*, 2014, **53**, 8442–8454.

29 T. Romero-Morcillo, M. Seredyuk, M. C. Munoz and J. A. Real, Meltable Spin Transition Molecular Materials with Tunable Tc and Hysteresis Loop Width, *Angew. Chem., Int. Ed.*, 2015, **54**, 14777–14781.

30 P. N. Martinho, Y. Ortin, B. Gildea, C. Gandolfi, G. McKerr, B. O'Hagan, M. Albrecht and G. G. Morgan, Inducing hysteretic spin crossover in solution, *Dalton Trans.*, 2012, **41**, 7461–7463.

31 P. N. Martinho, C. J. Harding, H. Müller-Bunz, M. Albrecht and G. G. Morgan, Inducing Spin Crossover in Amphiphilic Iron(III) Complexes, *Eur. J. Inorg. Chem.*, 2010, 675–679.

32 Y. Bodenthin, U. Pietsch, H. Möhwald and D. G. Kurth, Inducing Spin Crossover in Metallo-supramolecular Polyelectrolytes through an Amphiphilic Phase Transition, *J. Am. Chem. Soc.*, 2005, **127**, 3110–3114.

33 J. A. Kitchen, N. G. White, C. Gandolfi, M. Albrecht, G. N. L. Jameson, J. L. Tallon and S. Brooker, Room-temperature spin crossover and Langmuir–Blodgett film formation of an iron(II) triazole complex featuring a long alkyl chain substituent: the tail that wags the dog, *Chem. Commun.*, 2010, **46**, 6464.

34 P. Coronel, A. Barraud, R. Claude, O. Kahn, A. Ruaudel-Teixier and J. Zarembowitch, Spin transition in a Langmuir–Blodgett film, *J. Chem. Soc., Chem. Commun.*, 1989, 193–194.

35 K. Bairagi, O. Iasco, A. Bellec, A. Kartsev, D. Li, J. Lagoute, C. Chacon, Y. Girard, S. Rousset, F. Miserque, Y. J. Dappe, A. Smogunov, C. Barreteau, M.-L. Boillot, T. Mallah and V. Repain, Molecular-scale dynamics of light-induced spin cross-over in a two-dimensional layer, *Nat. Commun.*, 2016, **7**, 12212.

36 H. Soyer, E. Dupart, C. J. Gómez-García, C. Mingotaud and P. Delhaès, First Magnetic Observation of a Spin Crossover in a Langmuir–Blodgett Film, *Adv. Mater.*, 1999, **11**, 382–384.

37 H. Soyer, C. Mingotaud, M.-L. Boillot and P. Delhaes, Spin Crossover of a Langmuir–Blodgett Film Based on an Amphiphilic Iron(II) Complex, *Langmuir*, 1998, **14**, 5890–5895.

38 T. Fujigaya, D.-L. Jiang and T. Aida, Switching of Spin States Triggered by a Phase Transition: Spin-Crossover Properties of Self-Assembled Iron(II) Complexes with Alkyl-Tethered Triazole Ligands, *J. Am. Chem. Soc.*, 2003, **125**, 14690–14691.

39 O. Roubeau, J. M. Alcazar Gomez, E. Balskus, J. J. A. Kolnaar, J. G. Haasnoot and J. Reedijk, Spin-transition behaviour in chains of FeII bridged by 4-substituted 1,2,4-triazoles carrying alkyl tails, *New J. Chem.*, 2001, **25**, 144–150.

40 O. Roubeau, B. Agricole, R. Clérac and S. Ravaine, Triazole-Based Magnetic Langmuir–Blodgett Films, *J. Phys. Chem. B*, 2004, **108**, 15110–15116.

41 D. G. Kurth, P. Lehmann and M. Schutte, A route to hierarchical materials based on complexes of metallosupramolecular polyelectrolytes and amphiphiles, *PNAS*, 2000, **97**, 5704–5707.

42 S. Schlamp, P. Thoma and B. Weber, Influence of the Alkyl Chain Length on the Self-Assembly of Amphiphilic Iron Complexes: An Analysis of X-ray Structures, *Chem. – Eur. J.*, 2014, **20**, 6462–6473.

43 S. Schlamp, K. Dankhoff and B. Weber, Amphiphilic iron(ii) complexes with short alkyl chains – crystal packing and spin transition properties, *New J. Chem.*, 2014, **38**, 1965–1972.

44 S. Schlamp, P. Thoma and B. Weber, New Octahedral, Head-Tail Iron(II) Complexes with Spin Crossover Properties, *Eur. J. Inorg. Chem.*, 2012, 2759–2768.

45 S. Schlamp, B. Weber, A. D. Naik and Y. Garcia, Cooperative spin transition in a lipid layer like system, *Chem. Commun.*, 2011, **47**, 7152–7154.

46 W. Bauer, W. Scherer, S. Altmannshofer and B. Weber, Two-Step *versus* One-Step Spin Transitions in Iron(II) 1D Chain Compounds, *Eur. J. Inorg. Chem.*, 2011, 2803–2818.

47 W. Bauer, S. Schlamp and B. Weber, A ladder type iron(ii) coordination polymer with cooperative spin transition, *Chem. Commun.*, 2012, **48**, 10222.

48 B. Weber, R. Betz, W. Bauer and S. Schlamp, Crystal Structure of Iron(II) Acetate, *Z. Anorg. Allg. Chem.*, 2011, **637**, 102–107.

49 M. Tanner and A. Ludi, A facile synthesis of 4,4′-dipyridylacetylene, *Chimia*, 1980, **34**, 23–24.

50 K. Dankhoff, C. Lochenie, F. Puchtler and B. Weber, Solvent Influence on the Magnetic Properties of Iron(II) Spin-Crossover Coordination Compounds with 4,4′-Dipyridylethyne as Linker, *Eur. J. Inorg. Chem.*, 2016, 2136–2143.

51 B. Weber and E.-G. Jäger, Structure and Magnetic Properties of Iron(II/III) Complexes with $N_2O_2^{2-}$ Coordinating Schiff Base Like Ligands, *Eur. J. Inorg. Chem.*, 2009, 465–477.

52 B. Weber, Spin crossover complexes with N_4O_2 coordination sphere – The influence of covalent linkers on cooperative interactions, *Coord. Chem. Rev.*, 2009, **253**, 2432–2449.

53 C. Lochenie, K. Schötz, F. Panzer, H. Kurz, B. Maier, F. Puchtler, S. Agarwal, A. Köhler and B. Weber, Spin-Crossover Iron(II) Coordination Polymer with Fluorescent Properties: Correlation between Emission Properties and Spin State, *J. Am. Chem. Soc.*, 2018, **140**, 700–709.

54 C. Lochenie, J. Heinz, W. Milius and B. Weber, Iron(ii) spin crossover complexes with diaminonaphthalene-based Schiff base-like ligands: mononuclear complexes, *Dalton Trans.*, 2015, **44**, 18065–18077.

55 A. L. Spek, *PLATON – A Multipurpose Crystallographic Tool*, Utrecht University, Utrecht, The Netherlands, 2008.

56 C. Lochenie, W. Bauer, A. P. Railliet, S. Schlamp, Y. Garcia and B. Weber, Large Thermal Hysteresis for Iron(II) Spin Crossover Complexes with N-(Pyrid-4-yl)isonicotinamide, *Inorg. Chem.*, 2014, **53**, 11563–11572.

57 C. F. Macrae, P. R. Edgington, P. McCabe, E. Pidcock, G. P. Shilds, R. Taylor, M. Towler and J. van de Streek, Mercury, *J. Appl. Crystallogr.*, 2006, **39**, 453–457.

58 W. Bauer, T. Pfaffeneder, K. Achterhold and B. Weber, Complete Two-Step Spin-Transition in a 1D Chain Iron(II) Complex with a 110-K Wide Intermediate Plateau, *Eur. J. Inorg. Chem.*, 2011, 3183–3192.

59 B. Weber, E. S. Kaps, C. Desplanches, J.-F. Létard, K. Achterhold and F. G. Parak, Synthesis and Characterisation of Two New Iron(II) Spin-Crossover Complexes with N_4O_2 Coordination Spheres – Optimizing Preconditions for Cooperative Interactions, *Eur. J. Inorg. Chem.*, 2008, 4891–4898.

60 B. Weber, Mössbauer Spectra of FeII Spin crossover Complexes with N_4O_2 coordination sphere, *Moessbauer Eff. Ref. Data J.*, 2012, **35**, 238–254.

61 R. Nowak, W. Bauer, T. Ossiander and B. Weber, Slow Self-Assembly Favors Hysteresis above Room Temperature for an Iron(II) 1D-Chain Spin-Crossover Complex, *Eur. J. Inorg. Chem.*, 2013, 975–983.

62 B. Weber, E. S. Kaps, C. Desplanches and J.-F. Létard, Quenching the Hysteresis in Single Crystals of a 1D Chain Iron(II) Spin Crossover Complex, *Eur. J. Inorg. Chem.*, 2008, 2963–2966.

63 P. Gütlich, A. Hauser and H. Spiering, Thermal and Optical Switching of Iron(II) Complexes, *Angew. Chem., Int. Ed.*, 1994, **33**, 2024–2054.